

24 **Abstract**

25 We describe a method for measuring genome editing efficiency from *in silico* analysis of
26 high-resolution melt curve data. The melt curve data derived from amplicons of genome-
27 edited or unmodified target sites were processed to remove the background fluorescent
28 signal emanating from free fluorophore and then corrected for temperature-dependent
29 quenching of fluorescence of double-stranded DNA-bound fluorophore. Corrected data
30 were normalized and numerically differentiated to obtain the first derivatives of the melt
31 curves. These were then mathematically modeled as a sum or superposition of minimal
32 number of Gaussian components. Using Gaussian parameters determined by modeling of
33 melt curve derivatives of unedited samples, we were able to model melt curve derivatives
34 from genetically altered target sites where the mutant population could be accommodated
35 using an additional Gaussian component. From this, the proportion contributed by the
36 mutant component in the target region amplicon could be accurately determined. Mutant
37 component computations compared well with the mutant frequency determination from
38 next generation sequencing data. The results were also consistent with our earlier studies
39 that used difference curve areas from high-resolution melt curves for determining the
40 efficiency of genome-editing reagents. The advantage of the described method is that it
41 does not require calibration curves to estimate proportion of mutants in amplicons of
42 genome-edited target sites.

43 **Introduction**

44 Genome editing at predetermined loci has been greatly facilitated by new technologies
45 based on RNA-guided endonucleases (RGENs)[1-3] or transcription-activator like effector
46 nucleases (TALENs) [4-6]. The sequence-directed endonucleases introduce double-
47 stranded breaks (DSBs) at the target site. The DSBs can undergo two major types of DNA
48 repair. Non homologous end joining (NHEJ) repair results in indels at the cut site.

49 Homology-directed repair (HDR) either restores the original in the presence of an
50 endogenous template (sister chromatid) or inserts an exogenous DNA donor template
51 when available across the cut site [7-9].

52 The ability to generate genome-editing reagents with a desired specificity does not
53 guarantee efficient target site modification. There is therefore a need for methods that
54 rapidly assess reagent efficacy. A common approach is to determine efficacy of genome
55 editing reagents is to transfect human embryonic kidney (HEK293T) cell line with the
56 reagents. This is followed by amplification of target region by PCR and generation of
57 heteroduplexes by denaturation and renaturation in the presence of unmodified wild type
58 or different alleles. Mismatches in these heteroduplexes can be identified by digestion with
59 single-strand specific endonucleases (such as T7 or Surveyor nuclease) and resolution of
60 the digestion products in polyacrylamide or agarose gels [10-12].

61 A second approach to determine efficacy of genome editing is to use TaqMan assays with
62 probes designed to bind over the putative target cut site [12,13]. Reduced binding of the
63 TaqMan probe, due to indel mutations at the target site, with reference to a control
64 TaqMan probe that binds outside the cut site, can be used to estimate the editing efficacy.

65 A third method, which is gaining popularity, uses high resolution melting analysis (HRMA)
66 after real-time PCR with nonspecific double-stranded DNA (dsDNA)-binding dyes such as
67 Eva Green [12,14-16]. These dyes are more fluorescent when bound to dsDNA. In this
68 method, after amplifying the target region containing the repaired double-stranded break
69 site, the dsDNA is gradually warmed until the DNA completely melts. As dsDNA regions
70 melt into single-stranded regions, dye is expelled, decreasing the fluorescence signal.
71 Melting characteristics depend on the length of the PCR product, the sequence, and the
72 GC content. The temperature at which half of the DNA is single-stranded is called the T_m .
73 The T_m peak can be readily identified by first derivative transformations of melt curve

74 data. Target cut sites repaired by NHEJ generally exhibit lower Tms as the amplicons are
75 usually of smaller size than the wildtype target PCR product. We previously used HRMA to
76 estimate RGEN editing efficiency [12]. In that study, the region encompassing the target
77 site was amplified in a real-time PCR buffer and subjected to HRMA. Normalized melt
78 curves from genome-edited test samples were subtracted from control curves obtained
79 from unmodified targets to obtain difference curves. The difference curve areas (DCAs)
80 related directly to the percentage of mutants in the PCR product. We used standard
81 curves generated with mixes of wild type and mutant PCR products to accurately estimate
82 the percentage of mutants in different test samples. A major bottleneck to this method was
83 the requirement for a purely mutant PCR product to generate mixes for calibration curves.
84 Here we describe an alternative method that does not require standard curves to measure
85 the proportion of mutant species from high-resolution melt curve data. The high resolution
86 melt curves were first corrected for temperature dependent quenching of free and ds-DNA
87 bound fluorophore and then numerically differentiated to obtain first derivative melt curves.
88 First derivative melt curves from unmodified control target sites were modeled as sum of
89 two Gaussian components while edited samples were modeled using an additional
90 Gaussian component for the mutant population discernible in first derivative melt curves.
91 The weight of the "mutant" Gaussian component was shown to accurately reflect editing
92 efficiency of sequence-directed endonucleases.

93 **Materials & Methods**

94 **Cells**

95 Human embryonic kidney (HEK293T) cells were maintained in Dulbecco's modified
96 Eagle's medium containing 2 mM L-glutamine, 100 U/ml of penicillin, 100 µg/ml
97 streptomycin and 10% heat-inactivated fetal bovine serum (FBS)
98 (Hyclone/ThermoFisherScientific, USA) as described previously [17,18].

99 **Plasmids**

100 The plasmid constructs encoding TALENs targeting the c-c motif chemokine receptor 5
101 (CCR5, GenBank RefSeqGene number NG_012637) intron immediately downstream of
102 the coding exon have been described [12]. The dimeric guide RNA (dgRNA)-dCas9-FokI
103 system consists of pSQT1313 and pSQT1601 plasmids. pSQT1313 is used for expression
104 of dual guide RNAs (gRNAs) that target genomic DNA sequences on opposite strands and
105 spaced approximately 16 bases apart. pSQT1601 encodes dCas9-FokI fusion protein to
106 effect DSBs and Csy4 RNase to process the dgRNA expressed by pSQT1313. The
107 dgRNA-dCas9-FokI system was a gift from Keith Joung via Addgene.org. pSQT1313-
108 F8S2, targets the human coagulation factor VIII (F8) intron site 2 (F8-S2) and has been
109 previously described. The targeting/donor plasmid (pDonor-F8) or its backbone construct
110 (pBackbone) have also been described previously and encode a drug-resistance marker
111 that allows selecting transfected cells using puromycin.

112 **CaPO₄-mediated transfection**

113 Plasmids were introduced into sub confluent cultures of HEK293T cells in 6-well plates by
114 CaPO₄ -mediated transient transfection protocol as described previously [18]. Following
115 transfection, genomic DNA (gDNA) was isolated from unselected or puromycin-selected
116 populations using Qiagen DNeasy Blood and Tissue kit (Qiagen, Maryland, USA) as per
117 the recommended protocol.

118 **Amplification of target loci for obtaining high-resolution melt curves.**

119 This has been detailed in our earlier study [12]. Briefly, gDNA from genome-edited
120 samples was amplified using primer pairs SK144 and SK145 for the CCR5 locus, and
121 SK228 and SK229 for the F8-S2 locus, in Precision Melt buffer (Bio-Rad, USA). SK144
122 and SK145 generate a PCR product of size 107 bp. For some experiments we used a

123 different forward primer, SK214, that was located further upstream and produced a PCR
124 product of size 140 bp with reverse primer SK145. The sequences and genome locations
125 of these primers have been described earlier [12]. The gDNA from unmodified or mock-
126 transfected cells were also amplified in parallel using the same primer pairs. Post-
127 amplification melting of the PCR product was done between 65°C to 95°C in 0.2°C
128 increments.

129 **Processing melt curve data**

130 Relative fluorescence units (RFUs) of melt curve data were processed to correct for
131 background fluorescence of “unbound” fluorophore and for the temperature-dependent
132 quenching of dsDNA-bound fluorophore as described below.

133 For background fluorescence correction of unprocessed RFU, we used the post-melt
134 region of individual melt curves identified from plots of the raw RFU vs. temperature. We
135 plotted this region separately to obtain the parameters of a linear least squares fitting.
136 From this equation, we were able to extrapolate the background RFU at each of the
137 measured temperature points (Equation 1). Subtracting this value from the raw RFU gave
138 us the background subtracted RFU (BcRFU) (Equation 2).

139 The equations for background fluorescence correction of raw RFU:

Extrapolation of post-melt region using a first-order polynomial,

140
$$B_{pom}(x_i) = a \times x_i + b \quad (1)$$

where, x = temperature ($^{\circ}\text{C}$) and $T_{low} \leq x_i \leq T_{high}$

$$i = 1, 2, 3, \dots, \frac{(T_{high} - T_{low})}{0.2}; \quad x_{i+1} - x_i = 0.2 \text{ (temperature increment unit)}$$

T_{low} and T_{high} refer to the lower (e.g., 71°C) and higher (e.g., 95°C) limits

of the temperature range selected for melt curve analysis

The slope " a ", and the y-intercept " b " parameters are obtained

from first-order polynomial least-squares fitting of the post-melt region of the melt curve.

141 Background subtracted RFU, $BcRFU(x_i) = RFU(x_i) - B_{pom}(x_i) \quad (2)$

142 The pre-melt region of a melting curve identified from plots of melt curves of unmodified or
143 mock-transfected cells was used to determine the efficiency of detecting dsDNA-bound
144 fluorophore at different temperatures. This region of $BcRFU(x)$ of mock-transfected cells
145 was plotted separately and subjected to least squares curve fitting (Equation 3). The
146 curve-fitting equation was then used to extrapolate the values across the entire range of
147 temperatures encompassing the melting curve. The resulting values, representing
148 predicted RFU of unmelted DNA at the different temperatures, were then normalized to the
149 starting temperature (T_{low} or 71°C) to obtain the efficiency of detection of dsDNA-bound
150 fluorophore at each measured temperature point (Equation 4). The detection efficiency of
151 dsDNA-bound fluorophore derived from multiple mocks were averaged. The $BcRFU(x)$ of
152 mock or test samples were then divided by the average efficiency to obtain unquenched or
153 fluorescence-corrected RFU ($FcRFU(x)$) at each temperature point (Equation 5). The
154 $FcRFU(x)$ at T_{low} (71°C) was then used to normalize the melt curve to yield normalized
155 $FcRFU(x)$ or $nFcRFU(x)$ (Equation 6). First derivatives of $nFcRFU$, obtained by numerical
156 differentiation (Equation 7), were used for subsequent curve fitting analysis.

157 The mathematical formulations for correction of $BcRFU(x)$ for temperature-dependent
158 quenching of fluorescence of dsDNA-bound fluorophore are shown below.

159 Extrapolation of pre-melt region, $F_{prem}(x_i) = (c \times x_i + d)$ or $(c \times x_i^2 + d \times x_i + e)$ **(3)**

where, the parameters c, d, e were obtained from 1st-

or 2nd-order polynomial least squares fitting

of pre-melt region of $BcRFU(x)$

160 Efficiency of dsDNA detection at temperature x_i , $E(x_i) = \frac{F_{prem}(x_i)}{F_{prem}(x_i=71^\circ C)}$ **(4)**

161 Fluorescence corrected-RFU, $FcRFU(x_i) = \frac{BcRFU(x_i)}{E(x_i)}$ **(5)**

162 Normalized FcRFU, $nFcRFU(x_i) = \frac{FcRFU(x_i)}{FcRFU(x_i=71^\circ C)}$ **(6)**

(where $nFcRFU(x_i)$ represents dsDNA content ranging from 1 in the pre-melt region
to 0 in post-melt region)

163 The numerical differentiation of $nFcRFU(x)$ was carried out as follows:

164 $-\frac{d}{dT}(nFcRFU) \equiv -\frac{d}{dx}((nFcRFU(x_i)) = \frac{-(nFcRFU(x_{i+1})-nFcRFU(x_i))}{x_{i+1}-x_i} = \frac{-(nFcRFU(x_{i+1})-nFcRFU(x_i))}{0.2}$

165 **(7)**

166 **Gaussian decomposition of first derivatives melt curves of unedited** 167 **control samples**

168 Gaussian decomposition (GD) of first derivatives of $nFcRFU(x)$ was done using a
169 commercial software, CurveExpert Professional (V. 2.6, created by Daniel Hyams,
170 Madison, AL, USA). The normalized melt curve spans between zero and one and
171 resembles a cumulative probability distribution function. The first derivative of the
172 normalized melt curve resembles the density of probability distribution. A normal density
173 distribution is mathematically represented as:

174
$$\frac{1}{\sqrt{2\sigma^2\pi}} e^{-\frac{(x-\mu)^2}{2\sigma^2}} \quad (8)$$

175 where, μ is the center of the peak, σ is the standard deviation or SD (width at half-maximal
176 height of peak) and x is the temperature variable. For simplicity, we refer to this function
177 hereafter as Gaussian function or Gaussian in place of the more cumbersome "probability
178 density of normal distribution".

179 Since, the actual Gaussian function is of the form $ae^{-\frac{(x-\mu)^2}{2\sigma^2}}$, a corresponds to $\frac{1}{\sqrt{2\sigma^2\pi}}$ in
180 Equation 8 where the probability density distribution has been integrated and normalized
181 to one (the area under the curve).

182 For Gaussian modeling of derivative melt curves from unmodified control samples, the first
183 derivative of nFcRFU from mock-transfected (unmodified loci) samples were modeled as
184 either a single Gaussian function, $g_2(x)$:

185
$$g_2(x) = w_2 \frac{1}{\sqrt{2\sigma_2^2\pi}} e^{-\frac{(x-\mu_2)^2}{2\sigma_2^2}} \quad (9)$$

where, the free parameter w_2 represents the area under the curve or weight.

186 or as the sum of two Gaussian components, $g_2(x)$ and $g_3(x)$:

187
$$g_2(x) + g_3(x) = \left(w_2 \frac{1}{\sqrt{2\sigma_2^2\pi}} e^{-\frac{(x-\mu_2)^2}{2\sigma_2^2}} \right) + \left(w_3 \frac{1}{\sqrt{2\sigma_3^2\pi}} e^{-\frac{(x-\mu_3)^2}{2\sigma_3^2}} \right) \quad (10)$$

where, the Gaussian weights, $w_2 + w_3 = 1$ or $w_3 = 1 - w_2$.

188 The parameters μ_2 , and μ_3 , refer to the peak center or mean, and σ_2 and σ_3 refer to the
189 corresponding standard deviations (SDs) of Gaussian functions $g_2(x)$ and $g_3(x)$,
190 respectively. From curve fitting using the sum of two Gaussian functions ($g_2(x)$ and $g_3(x)$),
191 we were able to determine and 'fix' the parameters w_2 , w_3 , μ_2 , and μ_3 for subsequent
192 determination of percentage of mutants in genome-edited test samples (see below).

193 **GD of genome-edited samples**

194 For GD of derivative melt curves from genome-edited samples, the first derivative of
195 $nFcRFU(x)$ from test samples with genome-edited target loci were curve fitted as a sum of
196 either two Gaussian functions, $g1(x)$ and $g2(x)$ or as the sum of three Gaussian functions,
197 $g1(x)$, $g2(x)$ and $g3(x)$, where $g1(x)$ represents the contribution of the mutant population,
198 and $g2(x)$ and $g3(x)$ representing the contribution of the wildtype population in the PCR
199 amplicon of a given target site.

$$200 \quad g1(x) + g2(x) = \left(w_1 \frac{1}{\sqrt{2\sigma_1^2\pi}} e^{-\frac{(x-\mu_1)^2}{2\sigma_1^2}} \right) + \left((1 - w_1) \frac{1}{\sqrt{2\sigma_2^2\pi}} e^{-\frac{(x-\mu_{2fixed})^2}{2\sigma_2^2}} \right) \quad (11)$$

201 where, $w_1 + w_2 = 1$; the 'fixed' parameter μ_{2fixed} was determined from curve fitting of mock
202 samples using the single-Gaussian function, $g2(x)$, the other parameters were set free.

$$203 \quad g1(x) + g2(x) + g3(x) = \left(w_1 \frac{1}{\sqrt{2\sigma_1^2\pi}} e^{-\frac{(x-\mu_1)^2}{2\sigma_1^2}} \right) + \left(w_{2fixed}(1 - w_1) \frac{1}{\sqrt{2\sigma_2^2\pi}} e^{-\frac{(x-\mu_{2fixed})^2}{2\sigma_2^2}} \right) \\ + \left(w_{3fixed}(1 - w_1) \frac{1}{\sqrt{2\sigma_3^2\pi}} e^{-\frac{(x-\mu_{3fixed})^2}{2\sigma_3^2}} \right) \quad (12)$$

204 where, $w_1 + w_{2fixed}(1-w_1) + w_{3fixed}(1-w_1) = 1$, and w_{2fixed} , w_{3fixed} , μ_{2fixed} , and μ_{3fixed} were
205 determined from curve fitting of mock samples as the sum of two Gaussian functions,
206 $g2(x)$ and $g3(x)$, the other parameters were set free. The w_1 parameter determined from
207 curve fitting using either $g1(x) + g2(x)$ or $g1(x) + g2(x) + g3(x)$ functions represents the
208 mutant frequency in the amplicon.

209 **Curve fitting model comparison**

210 CurveExpert Professional outputs the corrected Akaike Information Criteria (AICc) values
211 for comparing curve fitting models - the model with the lower AICc value is deemed to

212 have the better fit. The relative likelihood was calculated using $e^{-0.5 \times (AIC_{C_{min}} - AIC_{C_i})}$ where
213 $AIC_{C_{min}}$ is the model with the lower of the two values and AIC_{C_i} is the value of the alternate
214 model. CurveExpert Professional also provides fitting "scores" for models, ranging from
215 zero to 1,000 with a higher score indicating a better fit. The score is in part based on
216 Akaike information criteria (AICc). The CurveExpert Professional scores were compared
217 using Student's t-test (paired, two-tailed).

218 **Results**

219 **High-resolution melt curve analysis**

220 The high-resolution melt curve data used here were generated in an earlier study [12].
221 Briefly, HEK293T were transfected with genome-editing reagents using a $CaPO_4$ method.
222 Two target regions were edited: F8 intron 1, and the CCR5 intron immediately downstream
223 of the coding exon. Although we targeted three distinct sites within the F8 intron in the
224 earlier study (referred to as sites F8-S1, -S2 or -S3), here we use data from genome-
225 edited F8-S2 only. We used TALENs for editing the CCR5 locus and dgRNA/dCas9-FokI
226 based RGEN system for editing the F8-S2 site. The gDNA, isolated from unselected or
227 selected populations of transfected cells, were amplified and high-resolution melt curve
228 data were obtained as described in Materials and Methods.

229 A high-resolution dsDNA melting curve consists of three regions: An initial pre-melt region
230 where the DNA is double-stranded, followed by a transition to more rapid decrease in
231 fluorescence attributable to DNA melting (melt region), and a second transition to a post-
232 melt region where the DNA strands are fully separated. The pre-melt region exhibits a
233 downward or negative slope with an increase of temperature prior to the transition to
234 melting. This decrease in fluorescence of dsDNA-bound fluorophore prior to the beginning
235 of separation of DNA strands can be attributed to temperature-dependent quenching of

236 fluorescence of dsDNA-bound fluorophore. The post-melt region also exhibits a downward
237 slope, albeit much shallower than the pre-melt slope. Since the post-melt region should
238 contain only unbound or free fluorophore, the decrease seen in this region can be
239 attributed to quenching effect of temperature on free or unbound fluorophore. Even after
240 correcting melt curve data for these two quenching phenomena, the resultant melting
241 curves of different samples frequently exhibit different pre-melt (starting) RFUs
242 necessitating a normalization step. The raw fluorescence, reported as relative
243 fluorescence units or RFU, therefore require processing and normalizing to enable
244 comparison of different melting curves and for decomposition into their Gaussian
245 components.

246 **Correction of RFU for temperature-dependent quenching of free** 247 **fluorophore**

248 To mathematically approximate free fluorophore behavior in the post-melt region, and to
249 determine the effect of temperature on fluorescence of free fluorophore over the entire
250 temperature range of melting, we first plotted the RFU vs. temperature in no template
251 controls (NTCs) used in the real-time PCR reactions (Fig. 1A). The NTC samples contain
252 all reactants except for the template gDNA. The RFU of free fluorophore in these reactions
253 exhibited a temperature-dependent linear decay in fluorescence across the entire
254 temperature range tested (Fig. 1A). These results validate extrapolating the post-melt
255 region to estimate background fluorescence from the unbound fluorophore to the earlier
256 temperature points (see below).

257

258 **Fig. 1** Temperature-dependent quenching of fluorescence of free and dsDNA-bound
259 fluorophore and its correction. (A) Plot of first-order polynomial curve fit of raw RFU vs.
260 temperature in no template controls (NTC). The equation shown in the plot is the mean \pm

261 SD of six different sample slopes and constants. (B) The unprocessed high-resolution
262 melting profile (blue trace) and the extrapolation from first-order polynomial curve fitting of
263 the post-melt curve region (red dashed line) from an amplicon of an unedited target site.
264 (C) High-resolution melting profile of background subtracted RFU (BcRFU, blue trace) and
265 that of 'unquenched' or fluorescence-compensated BcRFU (FcRFU, green trace) from an
266 unedited target site. The red dashed line shows extrapolation of pre-melt region from first-
267 order polynomial curve fitting of BcRFU and depicts the predicted BcRFU in the absence
268 of DNA melting. D) Comparison of first-order polynomial curve fitting of post-melt and pre-
269 melt portions of melting curves. Normalized data were used to enable plotting of the two
270 sets of data.

271

272 For correction of background fluorescence for each melt curve, we carried out first-order
273 polynomial curve fitting of the post-melt region of each melt curve data and then
274 extrapolated the background RFU values for earlier temperature data points (red dashed
275 line in Fig. 1B). We then subtracted the background RFUs corresponding to each
276 temperature point to obtain the background subtracted RFU or BcRFU as described in
277 Materials and Methods (Equation 2). The $BcRFU(x)$ melt curve is shown in Fig. 1C (blue
278 trace). The post-melt region of background subtracted-curve was nearly horizontal with an
279 RFU close to zero indicating that the background fluorescence from free or unbound
280 fluorophore was correctly computed and removed by this method.

281 **Correction of RFU for temperature-dependent quenching of dsDNA-** 282 **bound fluorophore**

283 To correct for quenching of fluorescence of dsDNA-bound fluorophore of background
284 subtracted melt curve data ($BcRFU(x)$), we carried out a regression analysis of the pre-
285 melt region of mock-transfected samples and extrapolated the RFUs across the range of

286 temperatures (red dashed line in Fig. 1C) (Equation 3). We obtained the efficiency of
287 detection of dsDNA-bound fluorophore by normalizing $F_{\text{prem}}(x)$ to the estimated RFU at the
288 starting temperature (T_{low} or 71°C) (Equation 4). The efficiency at each measured
289 temperature was then determined for multiple mock samples (Fig. 1D). Measured
290 efficiencies were nearly identical, diverging slightly at the higher temperatures, despite
291 determination across experiments conducted on different days, and with different samples.
292 The BcRFU of mock and test samples were divided by the average fluorescence efficiency
293 at each measured temperature to obtain fluorescence corrected $BcRFU(x)$ or $FcRFU(x)$ (
294 Fig. 1C, green tracing) (Equation 5). The pre-melt region was now rendered horizontal and
295 did not exhibit the temperature-dependent quenching profile of uncorrected melting
296 curves. For the F8-S2 target amplicon melt curve fitting with a first order polynomial
297 proved sufficient; for the CCR5 target amplicon melt curve, a second-order polynomial was
298 required (see below).

299 We next wished to directly compare the temperature-dependent quenching effect on
300 bound fluorophore vs. free fluorophore. To enable this comparison, we normalized the
301 extrapolated background RFUs (determined from individual post-melt curve data of
302 mocks) and plotted these along with the normalized bound-fluorophore efficiency (Fig.
303 1D). As anticipated from the NTC data shown in Fig. 1A, the slope of the free fluorophore
304 (-0.002) was much more shallow than that of the bound fluorophore (-0.04). Thus,
305 temperature-dependent fluorescence quenching of dsDNA-bound fluorophore is more
306 pronounced and significant than that of the unbound or free fluorophore.

307 **Rationale for Gaussian modeling of first derivate melt curves**

308 After high-resolution melt curve data were corrected for temperature-dependent quenching
309 of unbound and dsDNA-bound fluorophore, curves were normalized and then numerically
310 differentiated (Materials and Methods, Equations 6 and 7, respectively). When plotted, the

311 processed data showed that both the pre-melt and post-melt regions were squarely placed
312 on the zero baseline as expected (Fig. 2). The resulting peak of the first-derivate melt
313 curve data resembled a “bell” curve. Bell-shaped density distribution curves can result
314 from Cauchy-Lorentz, Student’s-t, Logistic or Gaussian distributions [19]. The Cauchy-
315 Lorentz density distribution has longer tails, while the Student’s-t and Logistic density
316 distributions exhibit heavier tails (kurtosis). The Gaussian distribution therefore seemed
317 more suitable for empirical modeling of first-derivative melt curves. A preliminary curve
318 fitting analysis using the Cauchy-Lorentz distribution function showed lower fit scores than
319 the Gaussian distribution function.

320

321 **Fig. 2** GD of first derivative of high-resolution melt curves of amplicons from gDNA of
322 unmodified target sites. gDNA from mock-transfected HEK293T cells (Mocks) were PCR
323 amplified using primer pairs targeting F8-S2 or CCR5 loci to obtain high resolution melt
324 curve data as described in Materials and Methods. The normalized and fluorescence
325 corrected melt curve data (nFcrFU) from F8-S2 (A and C) and CCR5 (B and D) target
326 sites were numerically differentiated as described in Materials and Methods (Equation 7).
327 1-GD (A and B) and 2-GD curve fitting of derivative melt curves were done using
328 CurveExpert Professional using Equation 9 and Equation 10, respectively. The first
329 derivative (y-axis: $-d(nFcrFU)/dT$) was plotted against temperature (x-axis) and is shown
330 as blue dots. The 1-GD curve fit to the first derivative data is shown as a red trace in A and
331 B. The individual Gaussians of 2-GD curve fit are shown as brown ($g_2(x)$) or green dashed
332 lines and their sum ($g_2(x) + g_3(x)$) is depicted as a solid red line in C and D. Table E
333 shows the Gaussian parameters determined from 1-GD curve fitting of A and B, while
334 Table F shows the parameters identified by 2-GD curve fitting of C and D using the
335 CurveExpert Professional software.

336 **Two-Gaussian decomposition is superior to one-Gaussian modeling of**
337 **derivative melt curves of unmodified target sites**

338 We first determined the parameters of the Gaussian components of first derivatives of
339 $nFcRFU(x)$ of unmodified or control samples (mocks) by curve fitting using the commercial
340 software CurveExpert Professional (Materials and Methods). Gaussian curve fitting
341 requires the user to input initial guesses for three of the parameters of a Gaussian
342 function: curve weight (w), curve center (μ), and width at half-maximal height (σ) or
343 standard deviation (SD). After multiple converging iterations using systematic changes to
344 the parameters of the model, the software finds parameters with the fitting accuracy
345 required or the maximum number of iterations is reached. The curve fitting output consists
346 of the curve-fitted weight (' w ' or area under the curve), curve center (μ) and the SD (σ).
347 The better the curve fit, the closer the weight or area under the curve approaches 1 for
348 derivatives of normalized melt curves.

349 We wished to use the simplest possible mathematical model for measuring the proportion
350 of mutant population in the amplicon of the target region. This would consist of one
351 Gaussian component for describing first derivative of $nFcRFU$ of unmodified mocks and
352 another Gaussian for the mutant population. The first derivative melting curves ($-$
353 $d(nFcRFU(x))/dx$) from unmodified F8-S2 and CCR5 loci (Fig. 2A and 2B) were curve fitted
354 using a single-Gaussian function, $g_2(x)$ (Materials and Methods, Equation 9). We refer to
355 this as single-Gaussian decomposition (1-GD). Modeling the first derivative of the F8-S2
356 target site showed the area under the curve had a weight (w_2) of 0.9537 ± 0.0021 . The
357 deviation of the fitted curve from the actual melt curve was clearly visible over the pre-melt
358 to melt transition region where the T_m of the amplicons with deletion mutations is situated
359 (Fig. 2A). 1-GD curve fitting for the CCR5 target was similar to that of F8-S2 target but with
360 only a slight divergence from the actual derivative melt curve (Fig. 2B). Consistent with this

361 the area under the curve was 1.003 ± 0.0039 (from four independent replicates). As in the
362 case of the F8-S2 target site, we saw a small divergence in the early melting region Fig.
363 2B ($g_2(x)$ vs. $-d(nFcRFU)/dT$).

364 Since the mutant molecules contribute to the melt profile in the early melt region, it was
365 necessary to ensure a more accurate curve fitting over this region than provided by a
366 single Gaussian component. To this end, we tested modeling of derivative melt curves of
367 unmodified controls as a sum of two Gaussian functions, $g_2(x) + g_3(x)$, (Materials and
368 Methods, Equation 10). As for the 1-GD curve fitting, we provided initial best guesses for
369 the five parameters (three for first Gaussian component and two for the second Gaussian
370 component). For the $g_3(x)$ Gaussian we suggested initial guesses for the mean (μ_3) over
371 the pre-melt/melt transition region. We stipulated that the sum of weights for w_2 and w_3
372 should equal one and set free w_2 (and thereby, $w_3 = 1 - w_2$). The results of this curve fitting
373 experiment are shown in Fig. 2C and 2D for the F8 and CCR5 loci, respectively. Unlike 1-
374 GD curve fitting, the sum of two Gaussian curve fitting (Fig. 2, $g_2(x) + g_3(x)$ indicated by a
375 red trace vs. $-d(nFcRFU)/dT$ indicated by blue dots) recreated the derivative melt curve
376 nearly perfectly. When we compared CurveExpert Professional scores (see Materials and
377 Methods, Comparing two curve fitting models), the two-Gaussian decomposition (2-GD)
378 model outscored the 1-GD model for both F8 and CCR5 mock samples (Table 1). This
379 difference, although slight, was statistically significant (paired Student's-t test, $p = 0.0000$).
380 The AICc values were lower for the 2-GD model indicating that it had a better fit. The
381 relative likelihood calculations from the AICc values of both 1- and 2-GD models, also
382 showed that 2-GD model was better (Table 1).

383

384 Table 1 2-GD model shows better fit than 1-GD for derivative melt curve data of mocks

Targeting Plasmid	Selection	Sample	1-GD score	2-GD score	1-GD AICc	2-GD AICc	Δ AICc	Relative likelihood
pBackbone	No	F8-S2 Mock 1	981	995	-625	-785	160	0.0000
pBackbone	No	F8-S2 Mock 2	982	995	-629	-795	166	0.0000
pDonor	No	F8-S2 Mock1	980	995	-620	-786	166	0.0000
pDonor	No	F8-S2 Mock 2	980	996	-618	-812	194	0.0000
pBackbone	Yes	F8-S2 Mock 1	978	996	-615	-813	198	0.0000
pBackbone	Yes	F8-S2 Mock 2	979	996	-618	-803	185	0.0000
pDonor	Yes	F8-S2 Mock 1	981	995	-629	-791	161	0.0000
pDonor	Yes	F8-S2 Mock 2	981	996	-625	-806	181	0.0000
None	No	CCR5 Mock 1	984	997	-732	-979	247	0.0000
None	No	CCR5 Mock 2	985	998	-748	-969	221	0.0000
None	No	CCR5 Mock 3	984	998	-729	-1057	328	0.0000

None	No	CCR5 Mock 4	983	997	-721	-990	268	0.0000
------	----	-------------	-----	-----	------	------	-----	--------

385

386 First-derivative melt curves from unmodified F8-S2 and CCR5 target sites provided distinct
387 Gaussian parameters from curve fitting as expected from their differing amplicon sizes,
388 sequences and differing Tms. Thus, they exhibited distinct centers or means for both 1-GD
389 (μ_2 of 79.19 ± 0.002 vs. 82.753 ± 0.087) (Table E in Fig. 2) and 2-GD fitting (μ_2 of $79.31 \pm$
390 0.017 vs. 82.898 ± 0.088 and μ_3 of 78.642 ± 0.013 vs. 82.265 ± 0.069 for F8-S2 and
391 CCR5, respectively) (Table F in Fig. 2). Likewise, they showed distinct differences in the
392 contribution of weights: w_2 of 0.954 ± 0.002 vs. 1.003 ± 0.004 in 1-GD fitting; and w_2 of
393 0.647 ± 0.006 vs. 0.587 ± 0.009 for F8-S2 and CCR5, respectively in 2-GD fitting. These
394 results highlight the requirement for determining Gaussian parameter values for each
395 target site from amplicons obtained from corresponding control or unmodified samples.

396 **Estimating percentage of mutants by GD of derivative melt curves from** 397 **genome-edited samples**

398 Comparing derivative melt curves of unmodified and genome-edited samples shows a
399 distinct mutant molecules' peak with a lower melting temperature (Fig. 2 vs. Fig. 3). *We*
400 *hypothesized that upon decomposition of the melting profile into its Gaussian components,*
401 *the area under the mutant peak would correspond to the proportion of mutant molecules in*
402 *the PCR product.* The Gaussian function representing the mutant population was
403 designated $g_1(x)$ in Equations 11 and 12 (Materials and Methods).

404

405 **Fig. 3** 3-GD of first derivative of high-resolution melt curves for estimation of mutant
406 percentage in genome-edited samples. gDNA was isolated from HEK293T cells
407 transfected with F8-S2 targeting RGENs or CCR5 targeting TALENs and PCR amplified
408 using corresponding primer pairs to obtain high resolution melt curve data (Materials and
409 Methods). 3-GD curve fitting was done on first derivative melt curves using CurveExpert
410 Professional and Equation 12 as described in Materials and Methods. The individual

411 Gaussians- $g_1(x)$ (purple dashed line), $g_2(x)$ (brown dashed line) and $g_3(x)$ (green dashed
412 line) and their sum- $g_1(x) + g_2(x) + g_3(x)$ (red solid line) were overlaid over the first
413 derivative melt curve (blue dots). GD of F8-S2 is shown in A and of CCR5 in B. Table C
414 shows the parameters (weights, centers and SDs) of 3-GD. The parameters that were
415 fixed from GD of mocks and those that were set free during 3-GD of edited samples are
416 shown in the Comments column. The g_1 weight (w_1) represents the mutation frequencies
417 in the amplicons of genome-edited F8-S2 and CCR5 target sites, respectively.

418

419 Since the better curve fitting of unmodified controls was obtained by using sum of two
420 Gaussian functions, we modeled derivative melt curves of test samples as a sum of three
421 Gaussian functions, $g_1(x) + g_2(x) + g_3(x)$ (Materials and Methods, Equation 12). The
422 parameters obtained from 2-GD of derivative melt curves of unmodified controls from F8-
423 S2 and CCR5 (means and weights) were then used to decompose corresponding test or
424 genome-edited samples. The different Gaussian components, $g_1(x)$, $g_2(x)$ and $g_3(x)$, and
425 their sum $g_1(x) + g_2(x) + g_3(x)$ are shown in Fig. 3. The predicted curve of the sum of the
426 three Gaussians was a near-perfect fit to the original derivative melt curve from test
427 samples (Fig. 3, $g_1(x) + g_2(x) + g_3(x)$, indicated by a red tracing vs. $-d(nFcRFU)/dT$ (Fig.
428 3, blue dots). The area under the g_1 curve, w_1 , of three-Gaussian decomposition (3-GD)
429 was deemed to represent the mutant population. The percentage of mutant population
430 estimated in amplicons of genome-edited F8-S2 and CCR5 target sites by 3-GD, shown in
431 Table C in Fig. 3, was $18.6 \pm 3.2\%$ vs. $23.2 \pm 8.7\%$, respectively. These results
432 demonstrate that first derivative melt curves from genetically altered sites can be modeled
433 successfully as a sum of three Gaussian functions.

434 Since the 1-GD of unedited samples was below the data points in the pre-melt to melt
435 transition region (Fig. 2), we hypothesized that 2-GD of genome-edited samples would

436 over estimate the mutant frequency. The results of these comparisons are shown in Fig. 4.
437 2-GD modeling estimated significantly higher mutant frequency than 3-GD modeling of
438 edited samples (Fig. 4A and 4B) as predicted.

439

440 **Fig. 4** Comparison of mutant percentage estimation by 2- and 3-GD. First derivatives of
441 high-resolution melt curves from genome-edited samples were curve fitted using 2- or 3-
442 GD models as described in Materials and Methods (Equation 11 and Equation 12,
443 respectively). The mutant percentages estimated from curve fitting are shown along the y-
444 axis for F8-S2 (A) and CCR5 (B). Two molecular clones (10 and 11) of dgRNAs targeting
445 F8-S2 site and two pairs of TALENs (L1R1 and L2R2) targeting CCR5 site were tested.
446 The mutant percentages were compared using Student's t-test (two-tailed). The p-values
447 of the pair-wise comparisons of 2-GD and 3-GD are shown above the bars.

448

449 Better curve fitting of 3-GD over 2-GD modeling was also revealed by the CurveExpert
450 Professional scores (Table 2). These differences were statistically significant (paired
451 Student's t-test, $p = 0.00001$). The AICc values were lower, indicating a better fit, for the 3-
452 GD model. Relative likelihood determinations from AICc values also revealed that the 3-
453 GD model was better. These results demonstrated that the 3-GD modeling was the
454 appropriate choice for GD of first derivative melt curves of amplicons of genome-edited
455 target sites.

456

457 **Table 2** 3-GD model achieves better fit than 2-GD for derivative melt curve data of genome-edited samples

F8-S2 site						CCR5 site					
2-GD Score	3-GD Score	2-GD AICc	3-GD AICc	Δ AICc	Relative likelihood	2-GD Score	3-GD Score	2-GD AICc	3-GD AICc	Δ AICc	Relative likelihood
979	992	-780	-911	131	0.0000	990	997	-837	-988	151	0.0000
990	996	-879	-1005	126	0.0000	985	995	-776	-907	130	0.0000
992	996	-923	-1008	85	0.0000	978	993	-733	-870	137	0.0000
983	994	-797	-949	153	0.0000	968	990	-690	-830	140	0.0000
990	995	-871	-978	108	0.0000	978	993	-728	-871	143	0.0000
992	996	-888	-1000	112	0.0000	973	992	-704	-857	154	0.0000
991	996	-869	-980	111	0.0000	972	992	-703	-851	148	0.0000
ND	ND			ND	ND	968	991	-681	-834	152	0.0000

458

459

460 **Comparison of GD method to prior approaches for measuring efficiency** 461 **of genome editing**

462 We next carried out 3-GD of high resolution melt curves of samples previously
463 characterized by NGS and by an alternative approach to measure mutant population
464 based on difference curve areas (DCAs) of normalized high-resolution melt curve profiles.
465 These samples exhibited a wide range of mutant percentages that were influenced by
466 puromycin drug selection and the use a donor template containing plasmid (pDonor-F8) or
467 its corresponding control plasmid (pBackbone) [12]. There were four categories of
468 samples: (1) pBackbone/Unselected, (2) pDonor/Unselected, (3) pBackbone/Selected,
469 and (4) pDonor/Selected. These four categories showed progressively increasing
470 percentages of mutations in the earlier study [12]. Two different clones of RGENs targeting
471 the F8-S2 site, clone 10 and clone 11, were tested. Clone 10 had previously exhibited
472 higher efficiencies than clone 11.

473 Results of curve fitting of derivative melt curves of mocks using 2-GD and of genome-
474 edited samples by 3-GD are shown for all the replicate samples in Fig. 5A. In all instances,
475 GD was able to accurately model the derivative melt curves including the mutant molecules'
476 peak. The area under this peak, w_1 , is shown as percentage within the plots. RGEN F8-S2
477 clone 10 edited samples showed higher percentages of mutants than clone 11. Drug-
478 selected samples exhibited higher mutant frequencies than corresponding unselected
479 samples and samples that received pDonor-F8 template (to effect homologous
480 recombination) exhibited higher mutant frequencies than corresponding samples that
481 received the control pBackbone plasmid.

482

483 **Fig. 5** Mutant frequency determination by 3-GD and comparison to difference curve areas
484 (DCAs) and next generation sequencing (NGS) data. HEK293T cells were transfected with

485 F8-S2 targeting dgDNA clone 10 (F8-S2 Cl.10) or clone 11 (F8-S2 Cl.11) together with a
486 dCas9-FokI construct. The cells were also cotransfected with either pBackbone or pDonor-
487 F8 targeting plasmids (Materials and Methods). Following transfection, gDNAs were
488 isolated from unselected cells or cells selected with puromycin and used for amplification
489 by PCR using appropriate primer pairs targeting F8-S2 loci to obtain high-resolution melt
490 curve data. (A) Mutant percentage estimations by 3-GD for the four different categories of
491 samples from unedited and edited F8-S2 site are identified on the left. The derivative melt
492 curves are shown as blue dots and the fitted curves from GD as red traces. Four PCR
493 replicates were analyzed for each clone with one exception (F8-S2 clone 10,
494 pBackbone/Unselected) for which only three replicates were tested. The mutant frequency
495 (percentage) estimated from the area of the mutant peak (w_1 parameter from $g_1(x)$), of 3-
496 GD) for each replicate is shown within the plot. (B-D) The average mutant frequency
497 determined by GD for the different categories in A were compared to mutant frequencies
498 determined by difference curve areas (DCA) (C) and to mutant frequency determination
499 from next generation sequencing (NGS). NGS was only done on unselected samples. (E)
500 Mutant frequency estimation from GD of high resolution melt curve data from gDNA of
501 HEK293T cells transfected with TALENs (two independent pairs of molecular clones
502 L1R1, L2R2) targeting CCR5 locus. CCR5 edited samples were also analyzed by NGS.
503 Error bar = 1 SD.

504

505 Direct comparison of the results with mutant frequency determination using DCA is shown
506 in Fig. 5B-C. Consistent with our previous observations, the percentage of mutants
507 estimated by both methods were within 3% of each other for both selected and unselected
508 samples (pBackbone or pDonor). There were two exceptions where the differences were
509 4.6% and 11.3%, respectively, with GD providing lower estimates. Possible explanations
510 for this discrepancy are provided in Discussion. The NGS of unselected samples treated

511 with pBackbone showed a similar trend as the above two methods (Fig. 5D) with clone 10
512 again showing higher efficiency of target site modification than clone 11. NGS generally
513 provided higher estimations of mutant frequencies than GD or DCA methods due to the
514 inclusion of insertion mutations in the calculations.

515 We used GD to also estimate the proportion of mutants in amplicons of samples edited at
516 the CCR5 locus. Here too, the results of GD and NGS showed similar trends (Fig. 5D).
517 These results *in toto* demonstrate that curve fitting of first derivative of high-resolution melt
518 curves is comparable to other methods used previously for estimating the proportion of
519 mutants in amplicons of genome-edited target sites. The results also indicate that one
520 could estimate mutant frequency percentages by GD for target sites for which there is no
521 ready availability of a 100% mutant population to generate calibration curves for the DCA
522 method (in this case genome-edited CCR5 target site).

523 **The size of the PCR product does not affect estimation of percentage of**
524 **mutants by GD from the same target locus despite exhibiting distinct**
525 **Gaussian parameters.**

526 We next wished to test if the size of the amplicon affected the estimation of percentage of
527 mutants. To this end, we amplified unmodified or genome-edited CCR5 target sites using
528 two sets of primers. The same antisense primer (SK145) was used for both PCR
529 amplifications but one of the sense primers (SK214) was situated further upstream of
530 primer SK144 so that the resulting amplicon sizes were 140 and 107 bp, respectively. GD
531 of high-resolution melt curves of both sizes of amplicons was done as above. Results are
532 shown in Fig. 6. The larger amplicon exhibited higher means (μ_1 , μ_2 and μ_3) for the three
533 Gaussian functions than the smaller one, as expected, and also showed distinguishable
534 SDs (Table 3). The percentages of mutants estimated from the larger or smaller PCR
535 product sizes determined by GD were 29.8 ± 1.1 % vs. 28.9 ± 8.6 %, respectively. The

536 values were not statistically significant (Student's t-test, $p \geq 0.05$). These results suggest
537 that small differences in amplicon sizes (less than 50 bp) do not affect the estimation of
538 genome-editing efficiency by GD.

539

540 **Fig. 6** Size of PCR product does not affect determination of mutant percentage by GD.

541 The CCR5 target site in gDNA of unmodified or genome-edited cells were amplified using
542 two pairs of primers designed to produce two distinct sizes of product (107 bp and 140 bp,
543 respectively). The amplicons were subjected to high-resolution melting and then
544 processed to correct for temperature-dependent quenching of fluorescence of free and
545 dsDNA-bound fluorophore. The resulting melt curves of genome-edited (for clone pair
546 L1R1) and unmodified controls (Mock) are shown (A & C). Corresponding first-derivatives
547 of processed melt curves are shown in B and D. Replicates G1 and G2, A1 and A2 refer to
548 gDNA samples amplified using primers that produce 107 bp amplicon, whereas G5 and
549 G6, and A5 and A6 refer to gDNA samples amplified using primers that produce 140 bp
550 amplicon. The derivative melt curves were decomposed using the 3-GD model to estimate
551 the mutant frequency. The estimated mutant frequencies for both sizes of amplicons are
552 shown in (E). Error bar = 1 SD.

553

554 **Table 3** Parameters determined by 3-GD of two different size amplicons from the CCR5-
555 edited target site

Gaussian Parameters	107 bp PCR product	140 bp PCR product
W_1 (%)	29.8 ± 1.1	28.9 ± 8.6
μ_1	79.8 ± 0.23	82.1 ± 0.19
σ_1	1.88 ± 0.20	1.07 ± 0.26
w_2	0.49 ± 0.01	0.48 ± 0.06
μ_2	82.8	84.2
σ_2	0.57 ± 0.01	0.51 ± 0.01
w_3	0.21 ± 0.00	0.24 ± 0.03
μ_3	82.1	83.6
σ_3	0.77 ± 0.05	0.65 ± 0.12

556

557

558 **Discussion**

559 Here we outline a method for estimating the efficiency of genome-editing reagents by GD
560 of high-resolution melt curve data. An initial pre-processing of the raw melt curve data was
561 required to correct for the quenching effect of temperature on measurement of
562 fluorescence as a prelude to GD for estimating the genome-editing efficiency. Our
563 approach consisted of two separate steps for correcting melting curves for temperature-
564 dependent quenching of fluorophore. The initial step of cleaning the data involved

565 removing the background fluorescence emanating from the free or unbound fluorophore.
566 Two methods have been used for this purpose. The first is to use an arbitrary cutoff point
567 in the post-melt region of the raw melt curve and subtract this value from all upstream
568 RFUs. We found that this method sometimes resulted in a small but narrow tail in the post-
569 melt region of the curve before it hit the baseline. This discrepancy could affect curve
570 fitting of the first derivative of the processed melt curve. The tail also hinted at a
571 temperature-dependent quenching of the free fluorophore. We confirmed this quenching
572 from linear regression analysis of no template controls used in PCR across the entire
573 range of melting (Fig. 1). The computed background RFU from linear regression of the
574 post-melt region of individual melt curves was used to effectively subtract the effect of free
575 fluorophore on the melt curve.

576 The second step to processing the melt curve involved correcting for temperature-
577 dependent quenching of the dsDNA-bound fluorophore evidenced in the pre-melt region.
578 As for the post-melt region, regression analysis of the pre-melt region can be used to
579 determine the efficiency of fluorescence of the dsDNA-bound fluorophore at any
580 temperature point along the melt curve profile. While detection efficiency can be computed
581 for individual melt curve profiles, we found that the temperature range of the pre-melt
582 region could be much shorter for some genome-edited samples due to the expected lower
583 T_ms for deletion mutations. For example, the pre-melt regions were only nominally present
584 for drug-selected samples that had a very high proportion of mutant molecules in the
585 amplicon (Fig. 5). In this case the mutant population constituted more than 90% of the
586 PCR product.

587 We found that for a given target, and pair of primers, the efficiency of detection of dsDNA-
588 bound fluorophore could be computed accurately and solely from unmodified or mock-
589 transfected samples. These efficiencies could not be distinguished from those estimated
590 from the individual test samples where sufficient pre-melt region was present (Fig. 1D).

591 We therefore chose to determine bound fluorophore detection efficiency from replicates of
592 mock-transfected samples and averaging them. Correction for the quenching of
593 fluorescence of dsDNA-bound fluorophore could be simply achieved by dividing the
594 $BcRFU(x)$ by the detection efficiency, $E(x)$ (Materials and Methods, Equation 4). This
595 process effectively eliminated the downward slope of the pre-melt region (Fig. 1C).

596 The temperature-dependent decay of fluorescence of dsDNA-bound fluorophore could be
597 modeled using either a first- or second-order polynomial function. For CCR5 samples, the
598 pre-melt region, following a correction using a first-order polynomial, showed a gentle
599 upward trajectory (saddleback pre-melt region) indicating that the RFU was not
600 compensated appropriately. Estimating the dsDNA-bound fluorophore efficiency using a
601 second-order polynomial curve fitting of the pre-melt region eliminated this artifact. From
602 this one can surmise that the fluorescence decay of dsDNA-bound fluorophore at higher
603 temperatures is better modeled with a second-order polynomial.

604 Correction for temperature-dependent quenching of fluorophores has been described
605 previously. Watras et al., found that fluorescence of chromophoric dissolved organic
606 matter (CDOM) decreased as ambient water temperature increased [20]. They suggested
607 compensating for the quenching using the equation:

$$608 \quad CDOM_r = \frac{CDOM_m}{[1 + \rho(T_m - T_r)]} \quad (13)$$

609 where t = temperature ($^{\circ}\text{C}$), r = reference and m = measured values, the coefficient, ρ , is
610 the quotient of slope divided by the intercept. The actual coefficient value, ρ , was found to
611 be instrument-dependent. A similar approach was recommended by Ryder et al [21,22].

$$612 \quad CDOM_{ref} = (CDOM_{meas} \times [1 + f_t(T_{ref} - T_{meas})]) \quad (14)$$

613 where f_t is the temperature correction coefficient, ref and $meas$ refer to reference and
614 measured temperatures. The two formulae for calculating fluorescence compensation

615 were shown to be mathematically identical [23]. This correction method is comparable to
616 our approach. Our initial attempts at correction for the quenching effect was to determine
617 the slope of pre-melt region and use it in place of the coefficient, ρ , in Equation 13. This
618 was combined with a simple baseline cut off for correction of melt curve data. We,
619 however, prefer first-order polynomial curve fit to determine and subtract the background
620 from individual melting curves, and then correct for the quenching effect of temperature on
621 dsDNA-bound fluorophore by dividing with the efficiency of detection of dsDNA determined
622 from unmodified controls. Both approaches should provide comparable results for
623 subsequent curve fitting after numerical differentiation. Our approach eliminates the
624 requirement for slope determination of the pre-melt region for each of the test samples
625 easing computation.

626 Palais and Wittwer described two methods for background correction [24]. 1) A baseline
627 method:

$$628 \quad M(T) = \frac{F(T) - L_0(T)}{L_1(T) - L_0(T)} \quad (15)$$

629 where, $M(T)$ is the corrected melt curve, $F(T)$ is the experimentally obtained melt curve,
630 and $L_1(T)$ and $L_0(T)$ refer to linear equations describing pre-melt and post-melt regions of
631 the curve, respectively. Thus, $M(T)$ corresponds to $F_cRFU(x)$, $F(T)$ to $RFU(x)$, $L_1(T)$ to
632 $F_{pre}(x)$ and $L_0(T)$ to $B_{pom}(x)$ of this study.

633 2) They also described an exponential background subtraction model:

$$634 \quad F(T) = M(T) + B(T) \quad (16)$$

$$\text{Where the background, } B(T) = Ce^{a(T-T_L)}$$

C and a are determined as described in detail in their publication.

635 The exponential background correction is recommended by Palais and Wittwer for
636 experiments involving multiple small amplicons and unlabeled probes, and also where the

637 pre- or post-melt regions of melt curve exhibit a concavity. We evaluated the exponential
638 background subtraction method to process the raw melting curve data for amplicons of F8-
639 S2 and CCR5 loci in unedited mock samples. The results are shown in Figs. 7A and 7B
640 and indicate that this correction method only partially compensated for the quenching
641 observed in the pre-melt region. Since the mutant population encroaches on pre-melt
642 region and extends into the melt transition portion, we abandoned this approach for
643 preprocessing the high-resolution melt curves.

644

645 **Fig. 7** Comparison of different methods of processing melt curve data for background and
646 fluorescence quenching correction. Melt curve data from amplicons of unmodified or
647 control samples from F8-S2 (A) or CCR5 target loci (B) were either unprocessed ($-dF/dT$,
648 blue trace) or corrected using exponential background subtraction method of Palais and
649 Wittwer (24) ($-dF/dT-dB/dT$, red dashes) or the method described in this study ($-$
650 $d(nF_cRFU)/dT$, green trace).

651

652 Our method for preprocessing melt curve data is mathematically indistinguishable from the
653 simpler baseline model of Palais and Wittwer (Equation 15). One difference between the
654 Palais and Wittwer method and our method is that we first subtract background emanating
655 from unbound fluorophore before correcting for efficiency of detection of dsDNA-bound
656 fluorophore. The second difference is that we formulate the decrease in fluorescence of
657 the pre-melt region not as a background problem but rather as an issue of detection
658 efficiency. The third difference is that the quenching of dsDNA-bound fluorophore was
659 modeled using either a first- or a second-order polynomial function depending on the
660 particular target amplicon. The final difference is that we determined ds-DNA bound

661 fluorophore detection efficiencies from control or mock samples and applied those to
662 correct melt curves of genome-edited samples.

663 After preprocessing melt curve data, we used GD to successfully model first derivative
664 melt curves. Cuellar and coworkers were amongst the earliest investigators to analyze
665 high-resolution denaturation profiles of reassociated repetitive DNA sequences using a
666 combination of higher derivative analysis and curve fitting [25]. They were able to
667 distinguish "thermal classes" of repetitive DNA duplexes exhibiting different amounts of
668 base pair mismatch in reassociated DNA. Reassociated *Escherichia coli* DNA exhibited a
669 single thermal class while pea and mung bean re-associated DNAs showed five distinct
670 thermal classes. These investigators obtained the first to fifth derivatives of the melting
671 profiles by numerical differentiation followed by smoothing using nine-point running
672 averages. For curve fitting of first derivative curves they used a software program called
673 RESOLV. Their results showed that the number of peaks identified by RESOLV
674 corresponded well with the fifth derivative of the melting profiles of reassociated mung
675 bean or pea DNAs. While these investigators were able to use an empirical approach to
676 identify multiple Gaussian components in reassociated DNA of legumes, they were unsure
677 if the components corresponded to populations of distinct sequences.

678 Moore and Gray proposed a method dubbed derivative domain fitting for resolving a
679 mixture of normal distributions in the presence of a contaminating background [26]. They
680 proposed this model for analyzing flow cytometric data. A requirement for decomposition
681 was that Gaussian peaks had to be separated by an SD greater than two. They mentioned
682 difficulties in accurately modeling the background by their method. While their approach is
683 an example of GD of data, their study is not directly comparable to ours.

684 Nellåker and coworkers proposed a *mixture model* to analyze of melting temperature data
685 [27]. The premise of their model is that distinct T_m categories indicate presence of

686 population of unique sequences. The "mixture model" allows calculating the proportions of
687 amplicons contributing to the distinct T_m categories identified in the mixes. Nellåker and
688 coworkers state that their *mixture model* actually denotes *mixture distributions* of statistical
689 distributions that arise from sampling of mixed populations. They formulate the probability
690 density function, $g(x)$ as follows:

$$691 \quad g(x) = \pi_1 f_1(x) + \dots + \pi_k f_k(x) \text{ where } 0 \leq \pi_i \leq 1, i = 1 \dots k, \pi_1 + \dots + \pi_k = 1 \quad (17)$$

692 The parameters $\pi_1 \dots \pi_k$ are referred to as the mixing weights or proportions. They applied
693 the mixture models to T_m data assuming it to consist of normally distributed components
694 with each component having the same standard deviation. They used a Gaussian
695 distribution function for their model. Thus, the function $g(x)$ (Equation 17) was represented
696 as:

$$697 \quad g(x) = \sum_{i=1}^k \pi_i \frac{1}{\sigma\sqrt{2\pi}} e^{-\frac{(x-\mu_i)^2}{2\sigma^2}} \quad (18)$$

where, x refers to temperature, and μ_i refers to
T_m of individual components of the mixture

698 The sum of Gaussian functions that we used in this study (Materials and Methods,
699 Equations 9 and 10) to curve fit the first derivative of processed melt curves, is similar to
700 that of Nellåker and coworkers. However, Nellåker and coworkers used their Gaussian
701 function for modeling T_m distributions of individual components of their mixture and did not
702 apply it to derivative transformations of melt curves of mocks. Here, we *apply the sum of*
703 *Gaussian functions to empirically reproduce the shape of the first derivative of high-*
704 *resolution melt curves for both mocks (sum of two Gaussians) and genome-edited*
705 *samples (sum of three Gaussians). A second difference is that we did not assume the SD*
706 *was the same for the decomposed Gaussian components. They were designated as*
707 *separate parameters for each Gaussian and set free during the modeling. However both*

708 Gaussian models sought to measure the proportion of particular component of the mixes,
709 the only difference being, we designated the weight of the different components as w_{1-3}
710 instead of π_i . This also eliminated possible confusion between the weight coefficient and
711 the mathematical constant π . In our case too, the sum of the weights of the Gaussian
712 components of first derivative melt curves equaled one.

713 Mann et al., also used a Gaussian model to curve fit melt curve derivatives [28]. They
714 were interested in automating the screening of first derivative melt curves following PCR to
715 detect products with unusual or aberrant melt curves to rapidly eliminate those samples
716 from further analyses. They used a different background correction method than those
717 described above. Their approach provides a pure Gaussian after subtraction of a sigmoid
718 shaped background fluorescence that does not retain the granularity of the derivative melt
719 curve from genome-edited target sites. In our model, the shape of the derivative melt
720 curve is critical for the precise quantitative decomposition into its Gaussian components.

721 There was good correspondence between the results obtained by GD and our earlier
722 described method based on DCAs for estimating mutant amplicon frequency (Fig. 5). The
723 DCA method was previously validated from NGS of the same amplicons. While the GD
724 and DCA methods yielded comparable estimation of editing efficiencies, there were a few
725 exceptions for amplicons consisting almost entirely of mutant species (Fig. 5A vs. 5B,
726 pDonor/Selected samples). We know, from our earlier study using a TaqMan assay, that
727 these gDNA samples have no detectable wildtype amplicons. Our explanation for this
728 anomaly is that 3-GD of nearly pure mutant amplicons (Equation 12) generates Gaussians
729 that overlap with those of mocks (Fig. 5A). In support of this hypothesis is our earlier
730 finding that indels with sufficiently large insertions can mimic wildtype molecules in HRMA
731 and constitute less than 10%. It is rather unlikely for mutant frequencies to approach such
732 high levels in transient transfection experiments in the absence of drug selection. We

733 therefore believe that this would not pose a significant hurdle for the GD model for
734 estimation of editing efficiencies.

735 During GD of mocks, we were intrigued by the small discrepancy in the derivative melt
736 curves at the melt transition temperature seen in single-Gaussian modeling. This seemed
737 more pronounced in F8-S2 samples. We hypothesized that in F8-S2 amplicons, there
738 were regions of the sequence that melted sooner or behaved as a nearly independent
739 domain that was AT-rich. To identify these regions in the sequence, we wrote a Python
740 function that determined the percentage of As and Ts in sliding windows of 10-mers that
741 shifted by one nucleotide. The moving averages (period = 5) are shown in Fig. 8A and 8B
742 (green traces). In the F8-S2 sequence, two initial broad regions with high AT content were
743 visible (Fig. 8A). In contrast, in the CCR5 sequence, few AT-rich regions that seemed
744 narrower were seen (Fig. 8 B).

745

746 **Fig. 8** Analysis of F8-S2 and CCR5 target sequence features and melting properties *in*
747 *silico*. Sliding window analysis of percentage of AT (%AT) in F8-S2 (A) or CCR5 (B)
748 sequences of target sites amplified by PCR. The percentage of As and Ts were
749 determined in a sliding overlapping window of 10-mers. The shift was by 1 bp. These are
750 shown as green dashes. The data was smoothed using running averages with a period of
751 5 (solid green line). The sum of free energies (ΔG_s) in a sliding window of 10-mers and a
752 shift of 1 bp is shown along the left y-axis in kJ/mol (blue dots). The running averages
753 were calculated as for %AT traces and are shown as blue traces. Putative AT-rich
754 domains are marked I-IV. (C- H) The F8-S2 and CCR5 target sequences were used as
755 input in the UMelt web analysis tool (29). UMelt predicted derivative melt curve (C and D),
756 "Dynamic Profile" of melting (E and F) using a sliding temperature control that was situated
757 close to the predicted T_m for each sequence to identify portions of the target sequences

758 (nucleotide position indicated on the x-axis) that may have melted earlier than the rest.

759 The web tool also provided a "Melting Profile" analysis that shows potential regions that

760 might show greater tendency to melt earlier (G and H).

761

762 We wrote another Python function to compute the free energy of a 10-mer sequence

763 window by using the nearest-neighbor method. For this analysis too, we used a sliding

764 window that shifted by one nucleotide. The moving averages (period =2) are shown in Fig.

765 8 (blue traces). Again, the initial AT-rich region exhibited lower free energies (ΔG s) for F8-

766 S2 sequence than that of the CCR5 sequence (Fig. 8A and 8B).

767 We next used the online web tool uMelt [29] to determine if the melting profiles of F8-S2

768 and CCR5 amplicon sequences could be distinguished by *in silico* analysis. For F8-S2

769 amplicon, the derivative melt curve predicted by uMelt web tool, showed a bulge in the

770 early melt region (Fig. 8C). The Dynamic Profile window also predicted melting at earlier

771 temperatures at both ends, particularly at the 5' end of the sequence (Fig. 8D). The

772 Melting Profile pane (Fig. 8E) also showed increased melting at lower temperatures for the

773 first 50 base pairs. In contrast to F8-S2, for the CCR5 target sequence amplicon, the web

774 tool predicted only a small deviation of melt curve in the early melt region (Fig. 8F). The

775 Dynamic Profile (Fig. 8G) for CCR5 target amplicon also showed nearly equal rates of

776 melting from both ends of the sequence with a barely visible enhancement for the left end.

777 Likewise, the Melting Profile pane (Fig. 8H) showed very little propensity for a separate

778 domain that exhibited different melting characteristics than the rest of the sequence for

779 CCR5. The differences noted between the predicted derivative melt curves and the

780 experimentally derived counterparts have been attributed to uMelt software being based

781 on ΔG s determined for pairs of nucleotides using a spectrophotometric method rather than

782 on fluorescence emission from the binding of dsDNA-binding fluorophores. Nevertheless,

783 uMelt analysis supports the two-Gaussian model for curve fitting of unmodified control
784 samples.

785 In conclusion, this paper describes a method to correct high-resolution melt curves for
786 temperature-dependent quenching of free and dsDNA-bound fluorophore. This is the first
787 report, to the best of our knowledge, to demonstrate that first derivative melting curves of
788 properly processed high-resolution melt curve data can be precisely modeled as a sum or
789 superposition of Gaussian functions. The GD model successfully estimated efficiency of
790 genome-editing by engineered sequence-directed endonucleases without a requirement
791 for standard curves and has the additional advantage of being a single-tube method.

792 **Acknowledgments**

793 We thank the Division of Hematology-Oncology, Bone Marrow Transplant and Cellular
794 Therapy within the Department of Internal Medicine, Saint Louis University, for making
795 available facilities and funding to carry out the described work. We also thank Mike
796 Marcinkowski for editing the text and Matt Schuelke for reviewing the statistics used in
797 evaluating GD models.

798 **Supporting information**

799 Datasets containing Excel, Numbers (generated on Mac) and Jupyter Notebook files (for
800 running Python programs used in the manuscript) can be accessed at:
801 <https://figshare.com/s/4f07b851af468f18b42d>

802 **Bibliography**

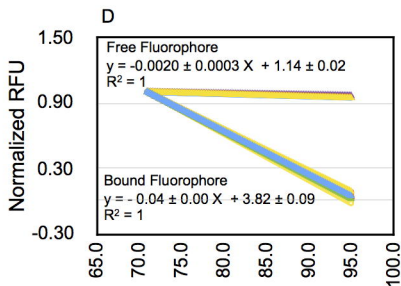
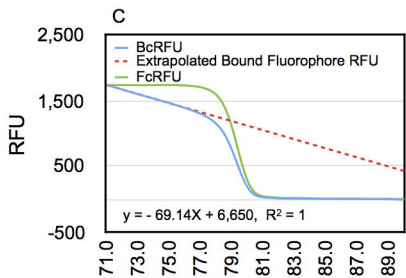
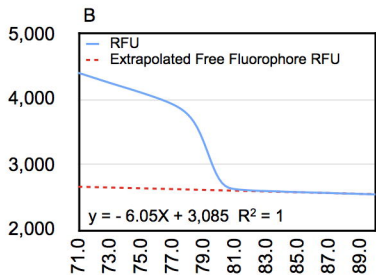
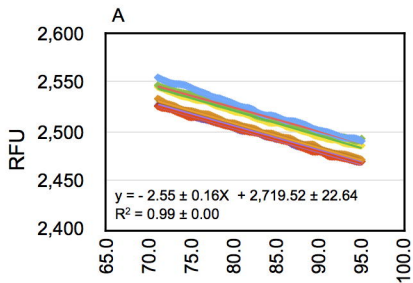
- 803 1. Ran FA, Hsu PD, Wright J, Agarwala V, Scott DA, Zhang F. Genome engineering
804 using the CRISPR-Cas9 system. *Nature Protocols*. 2013;8: 2281–2308.
805 doi:10.1038/nprot.2013.143
- 806 2. Sakuma T, Yamamoto T. CRISPR/Cas9: The Leading Edge of Genome Editing
807 Technology. *Targeted Genome Editing Using Site-Specific Nucleases*. Tokyo:

- 808 Springer Japan; 2014. pp. 25–41. doi:10.1007/978-4-431-55227-7_2
- 809 3. Kiani S, Chavez A, Tuttle M, Hall RN, Chari R. Cas9 gRNA engineering for genome
810 editing, activation and repression. *Nature*. 2015.
- 811 4. Glazkova DV, Shipulin GA. TALE nucleases as a new tool for genome editing. *Mol*
812 *Biol*. Pleiades Publishing; 2014;48: 305–318. doi:10.1134/S0026893314030054
- 813 5. Boch J. TALEs of genome targeting. *Nature Biotechnology*. *Nature Research*;
814 2011;29: 135–136. doi:10.1038/nbt.1767
- 815 6. Mussolino C, Cathomen T. TALE nucleases: tailored genome engineering made
816 easy. *Curr Opin Biotechnol*. 2012;23: 644–650. doi:10.1016/j.copbio.2012.01.013
- 817 7. Wyman C, Kanaar R. DNA Double-Strand Break Repair: All's Well that Ends Well.
818 *Annu Rev Genet*. 2006;40: 363–383. doi:10.1146/annurev.genet.40.110405.090451
- 819 8. Jacquet K, Côté J. DNA repair. *Cell Cycle*. Taylor & Francis; 2014;13: 1059–1059.
820 doi:10.4161/cc.28383
- 821 9. Symington LS, Gautier J. Double-Strand Break End Resection and Repair Pathway
822 Choice. *Annu Rev Genet*. 2011;45: 247–271. doi:10.1146/annurev-genet-110410-
823 132435
- 824 10. Zhu L, Mon H, Xu J, Lee JM, Kusakabe T. CRISPR/Cas9-mediated knockout of
825 factors in non-homologous end joining pathway enhances gene targeting in silkworm
826 cells. *Nature Publishing Group*. *Nature Publishing Group*; 2015;5: 1–13.
827 doi:10.1038/srep18103
- 828 11. Lin S, Staahl BT, Alla RK, Doudna JA. Enhanced homology-directed human genome
829 engineering by controlled timing of CRISPR/Cas9 delivery. *eLife*. 2014;3: 1314–13.
830 doi:10.7554/eLife.04766
- 831 12. Zaboikin M, Zaboikina T, Freter C, Srinivasakumar N. Non-Homologous End Joining
832 and Homology Directed DNA Repair Frequency of Double-Stranded Breaks
833 Introduced by Genome Editing Reagents. Hu W, editor. *PLoS ONE*. Public Library of
834 Science; 2017;12: e0169931. doi:10.1371/journal.pone.0169931
- 835 13. Miyaoka Y, Berman JR, Cooper SB, Mayerl SJ, Chan AH, Bin Zhang, et al.
836 Systematic quantification of HDR and NHEJ reveals effects of locus, nuclease, and
837 cell type on genome- editing. *Nature Publishing Group*. *Nature Publishing Group*;
838 2016;6: 1–12. doi:10.1038/srep23549
- 839 14. Parant JM, George SA, Pryor R, Wittwer CT, Yost HJ. A rapid and efficient method
840 of genotyping zebrafish mutants. *Dev Dyn*. Wiley-Liss, Inc; 2009;238: 3168–3174.
841 doi:10.1002/dvdy.22143
- 842 15. Thomas HR, Percival SM, Yoder BK, Parant JM. High-throughput genome editing
843 and phenotyping facilitated by high resolution melting curve analysis. Jennings B,
844 editor. *PLoS ONE*. 2014;9: e114632. doi:10.1371/journal.pone.0114632
- 845 16. Hill JT, Demarest BL, Bisgrove BW, Su Y-C, Smith M, Yost HJ. Poly peak parser:
846 Method and software for identification of unknown indels using sanger sequencing of
847 polymerase chain reaction products. *Dev Dyn*. 2014;243: 1632–1636.

- 848 doi:10.1002/dvdy.24183
- 849 17. Srinivasakumar N, Zaboikin M, Tidball AM, Aboud AA, Neely MD, Ess KC, et al.
850 Gammaretroviral vector encoding a fluorescent marker to facilitate detection of
851 reprogrammed human fibroblasts during iPSC generation. *PeerJ*. PeerJ Inc; 2013;1:
852 e224. doi:10.7717/peerj.224
- 853 18. Srinivasakumar N. Packaging cell system for lentivirus vectors. Preparation and use.
854 *Methods Mol Med*. 2002;69: 275–302.
- 855 19. Forbes C, Evans M, Hastings N, Peacock B. *Statistical Distributions*. Hoboken, NJ,
856 USA: John Wiley & Sons, Inc; 2010. doi:10.1002/9780470627242
- 857 20. Watras CJ, Hanson, P.C., Stacy TL, Morrison KM, Mather J, Hu YH, et al. A
858 temperature compensation method for CDOM fluorescence sensors in freshwater.
859 *Limnology and Oceanography: Methods*. 2011;9: 296–301.
860 doi:10.4319/lom.2011.9.296
- 861 21. Ryder E, Jennings E, de Eyto E, Dillane M, NicAonghusa C, Pierson DC, et al.
862 Temperature quenching of CDOM fluorescence sensors: temporal and spatial
863 variability in the temperature response and a recommended temperature correction
864 equation. *Limnology and Oceanography: Methods*. 2012;10: 1004–1010.
865 doi:10.4319/lom.2012.10.1004
- 866 22. Ryder E, Jennings E, de Eyto E, Dillane M, Nic Aonghusa C, Pierson DC, et al.
867 Reply to a comment by Watras et al. (2014) on temperature compensation method
868 for field measurements of CDOM fluorescence. *Limnology and Oceanography:*
869 *Methods*. 2015;13: 527–528. doi:10.1002/lom3.10045
- 870 23. Watras CJ, Morrison KA, Mather J, Milewski P, Hanson PC. Correcting CDOM
871 fluorescence measurements for temperature effects under field conditions in
872 freshwaters. *Limnology and Oceanography: Methods*. 2014;12: 23–24.
873 doi:10.4319/lom.2014.12.23
- 874 24. Palais R, Wittwer CT. Chapter 13 - Mathematical Algorithms for High-Resolution
875 DNA Melting Analysis. 1st ed. *Methods in Enzymology: Computer Methods, Part A*.
876 Elsevier Inc; 2009. pp. 323–343. doi:10.1016/S0076-6879(08)03813-5
- 877 25. Cuellar RE, Ford GA, Briggs WR, Thompson WF. Application of higher derivative
878 techniques to analysis of high-resolution thermal denaturation profiles of
879 reassociated repetitive DNA. *Proceedings of the National Academy of Sciences*.
880 National Academy of Sciences; 1978;75: 6026–6030.
- 881 26. Moore DH, Gray JW. Derivative domain fitting: a new method for resolving a mixture
882 of normal distributions in the presence of a contaminating background. *Cytometry*.
883 1993;14: 510–518. doi:10.1002/cyto.990140510
- 884 27. Nellåker C, Uhrzander F, Tyrcha J, Karlsson H. Mixture models for analysis of
885 melting temperature data. *BMC Bioinformatics*. 2008;9: 370–6. doi:10.1186/1471-
886 2105-9-370
- 887 28. Mann TP, Humbert R, Stamatoyannopolous JA, Noble WS. Automated validation of
888 polymerase chain reactions using amplicon melting curves. *Proc IEEE Comput Syst*
889 *Bioinform Conf*. 2005;: 377–385.

- 890 29. Dwight Z, Palais R, Wittwer CT. uMELT: prediction of high-resolution melting curves
891 and dynamic melting profiles of PCR products in a rich web application.
892 Bioinformatics. Oxford University Press; 2011;27: 1019–1020.
893 doi:10.1093/bioinformatics/btr065

894



Temperature

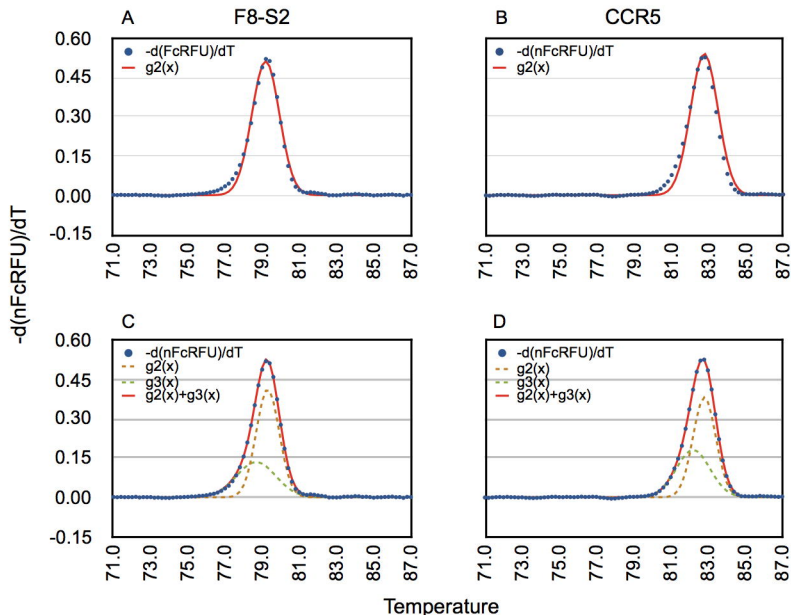


Table E. 1-GD parameters of derivative melt curves of controls

Gaussian Function	Parameters	F8-S2	CCR5	Curve Fitting Comments
g2(x)	g2 weight (w_2) (area under the curve)	0.954 ± 0.002	1.003 ± 0.004	Set free
	g2 center (μ_2) (T_m)	79.19 ± 0.002	82.753 ± 0.087	Set free
	g2 SD (σ_2) (width at half-maximal height)	0.738 ± 0.003	0.740 ± 0.008	Set free

Table F. 2-GD parameters of derivative melt curves of controls

Gaussian Function	Parameters	F8-S2	CCR5	Curve Fitting Comments
g2(x)	g2 weight (w_2)	0.647 ± 0.006	0.587 ± 0.009	Set free
	g2 center (μ_2)	79.31 ± 0.017	82.898 ± 0.088	Set free
	g2 SD (σ_2)	0.610 ± 0.011	0.618 ± 0.003	Set free
g3(x)	g3 center (μ_3)	78.642 ± 0.013	82.265 ± 0.069	Set free
	g3 SD (σ_3)	1.013 ± 0.048	0.907 ± 0.019	Set free
	g3 weight (w_3)	$1 - w_2$	$1 - w_2$	Set $w_3 = 1 - w_2$

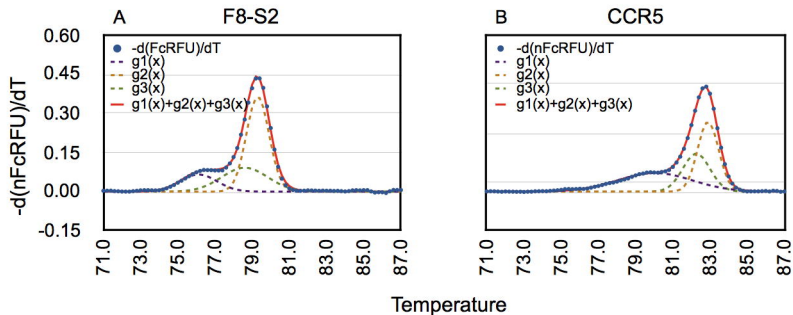
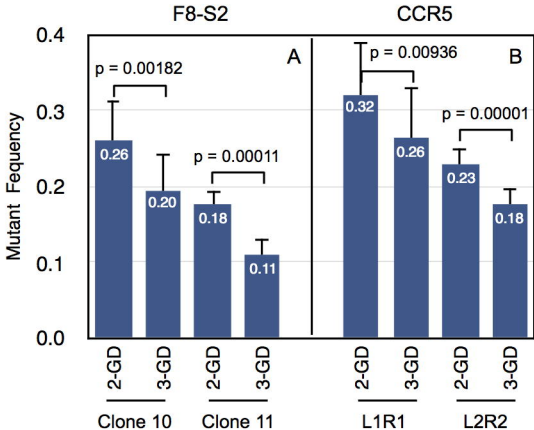
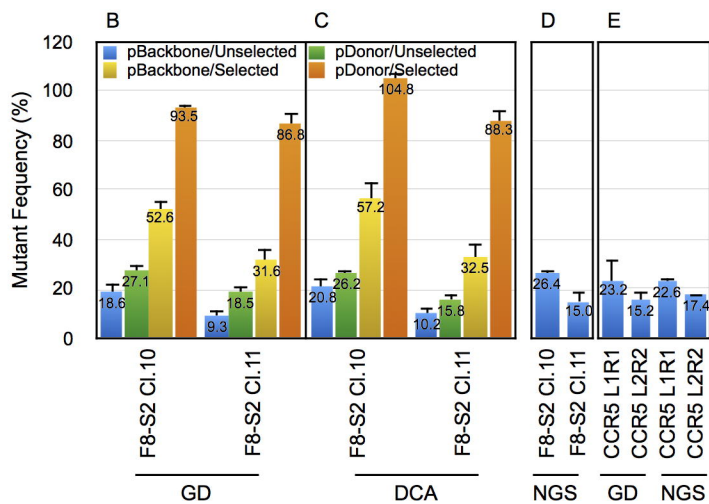
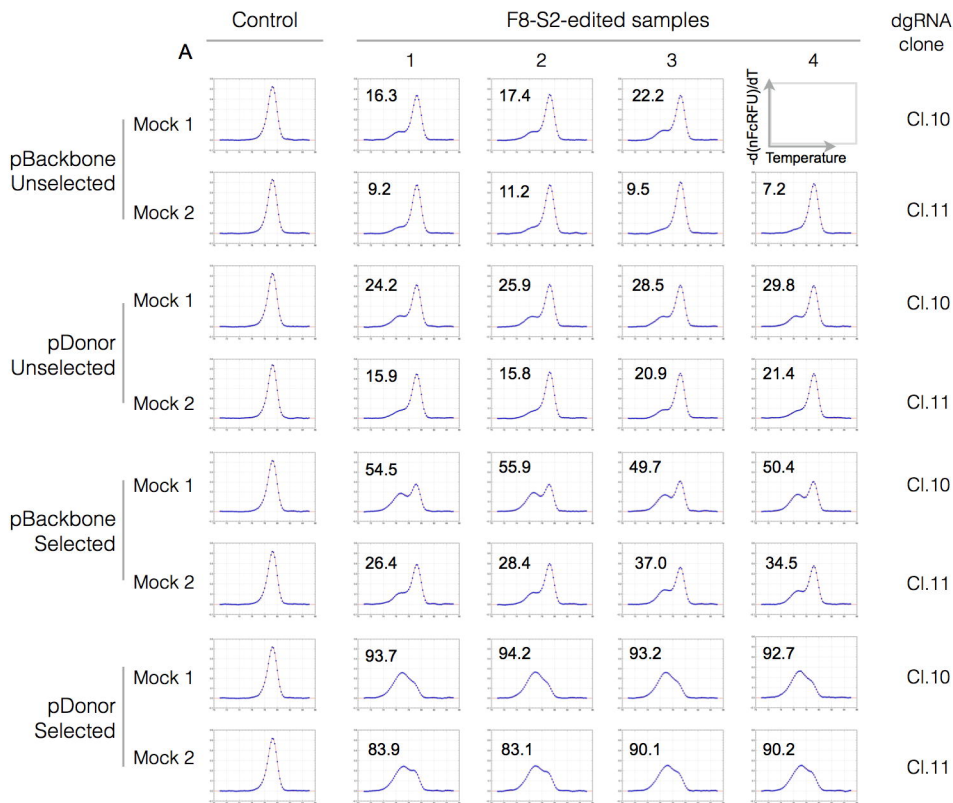
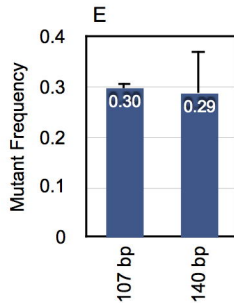
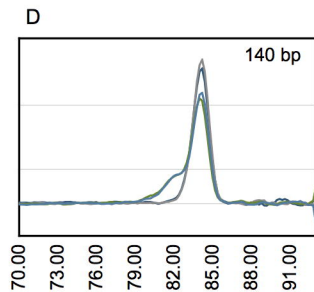
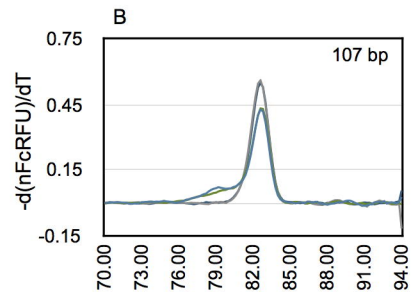
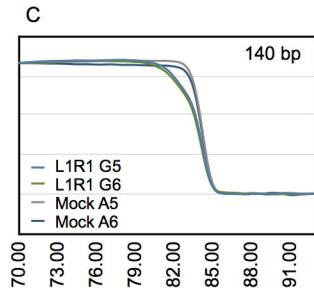
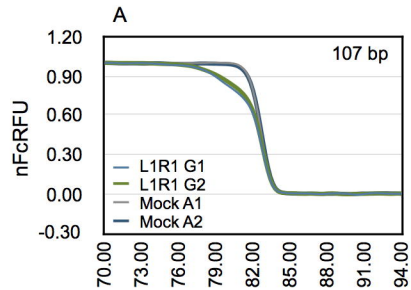


Table C. 3-GD parameters of derivative melt curves of genome-edited samples

Gaussian Function	Parameters	F8-S2 clone 10	CCR5 L1R1	Curve Fitting Comments
g1(x)	g1 weight (w_1)	0.186 ± 0.032	0.232 ± 0.087	Set free
	g1 center (μ_1)	76.228 ± 0.112	79.680 ± 0.307	Set free
	g1 SD (σ_1)	0.991 ± 0.004	1.392 ± 0.423	Set free
g2(x)	g2 weight ($w_{2\text{fixed}}$)	0.6607	0.5870	Average w_2 from mock
	g2 center ($\mu_{2\text{fixed}}$)	79.300	82.900	Average μ_2 from mock
	g2 SD (σ_2)	0.602 ± 0.010	0.574 ± 0.011	Set free
g3(x)	g3 weight ($w_{3\text{fixed}}$)	$1 - w_2$	$1 - w_2$	Average from mock ($1 - w_2$)
	g3 center ($\mu_{3\text{fixed}}$)	78.600	82.270	Average μ_3 from mock
	g3 SD (σ_3)	1.040 ± 0.186	0.899 ± 0.158	Set free







Temperature

